Unveiling the Effects of Sb or Bi doping on Lattice Strain and Raman spectra in Mg_2Si Single Crystals

Kosuke Shimano[1], Shunya Sakane[1], Takehiro Ota[2], Kenichiro Takakura[2], Motoharu Imai[3], and Haruhiko Udono[1*]

[1] *Graduate School of Science and Engineering, Ibaraki University, 4-12-1 Nakanarusawa, Hitachi, Ibaraki 316-8511, Japan*

[2] *National Institute of Technology (KOSEN), Kumamoto College, Koshi, Kumamoto 861-8081, Japan*

[3] *National Institute for Materials Science (NIMS), 1-2-1 Sengen, Tsukuba, Ibaraki 305-0047, Japan*

*E-mail: udono@vc.ibaraki.ac.jp

We thoroughly investigated Raman peaks of Sb- or Bi-doped Mg_2Si single crystals grown by the vertical Bridgman techniques, and clarified the relationship between Raman peak shift and lattice strain using first-principles calculations. Rietveld analysis of powder X-ray diffraction revealed that the lattice constant increased monotonically with Sb and Bi doping amounts. Raman spectroscopy demonstrated that the F_{2g} mode of Mg_2Si (near 258 cm^{-1}) shifted to lower wavenumbers with increasing doping amounts. This peak shift was mainly attributed to the lattice strain, which was revealed by the First-principles calculations. These findings provide the usefulness of Raman spectroscopy for Mg_2Si substrates.

1. Introduction

Mg_2Si, which has an anti-fluorite structure, is a semiconductor made of abundant non-toxic elements (Mg and Si). Its electronic band structure is an indirect transition type with a bandgap of 0.61 eV at room temperature, and it can be tuned from 0.57 eV to 0.36 eV by substituting Ge or Sn for Si, respectively. Therefore, it is expected to be used as a Si-based infrared sensor in the short-wavelength infrared region. In addition, it has relatively low thermal conductivity among silicide-based semiconductors, and some studies on its potential as a thermoelectric material have also been conducted.1-5) To explore the fundamental properties of these applications, it is important to grow high-quality single crystals.

Morris *et al.* (1958) reported on the electrical properties of Mg_2Si single crystals grown using graphite crucibles, investigating the electrical properties in the temperature range of 77-1000 K.6) Similarly, Heller *et al.* (1961) grew Mg_2Si single crystals and studied the Seebeck effect over a broader temperature range of 7-1000 K.7) We have also developed a VB (Vertical Bridgman) method for growing Mg_2Si single crystals.8-14) We have demonstrated that the purity of the Mg raw material affects the carrier transport properties in Mg_2Si single crystals, where the Hall mobility of 14,500 cm^2/Vs at 45 K was achieved with high-purity Mg raw material (6N-up-grade).8) Additionally, Mg_2Si single crystals without small-angle grain boundaries was produced by using a pyrolytic boron nitride (pBN) crucible coated with boron nitride.9) Using the high-purity n-type Mg_2Si substrate, we have fabricated a pn junction photodiode by thermal diffusion of Ag as an acceptor impurity and demonstrated a photoresponse below 2.1 μm.10-14)

In the future, when fabricating more precise devices using Mg_2Si as a substrate, stress evaluation of the substrate will be an important issue. Raman spectroscopy, a non-destructive and simple method, is effective to evaluate the stress of Mg_2Si easily. In the case of silicon, the relationship between the amount of Raman peak shift and strain is well-known and is actually used for strain evaluation.15,16)

The Raman spectrum of Mg_2Si is observed as a resonant scattering of the F_{2g} mode at around 258 cm^{-1}.17-22) Buchenauer *et al.* and Anastassakis *et al.* demonstrated that this peak shifts to higher wavenumbers and becomes steeper at low temperatures.19,20) Wang *et al.* conducted measurements under gas pressure and found that the wavenumber shift increases with pressure.23) Onari *et al.* investigated the Raman spectra of Mg_2Si single crystals under uniaxial stress along [111] and reported the shift and splitting of the F_2g peak.22) These peak shifts are suggested to be caused by changes in the force constant and tension. Furthermore, Yasseri *et al*. reported that the peak shifts to lower wavenumbers due to intermixing with Sn.[24)] In addition, Raman spectra of Al-doped Mg_2Si thin films[25)] and Sb-doped Mg_2Si single crystals has also been measured.[2)] These studies have focused on the detection of precipitates, and the peak shift has not been examined in detail. A comprehensive analysis of Raman peaks in impurity-doped Mg_2Si single crystals remains an important issue.

In this study, we thoroughly investigated Raman peaks of Sb- or Bi-doped Mg_2Si single crystals grown by the VB techniques, and clarified the relationship between Raman peak shift and lattice strain using first-principles calculations.

2. EXPERIMENTAL AND COMPUTATIONAL METHODS

2.1 Sample preparation

Undoped, Sb-doped, and Bi-doped Mg_2Si single crystals were prepared by the VB method. Undoped Mg_2Si was prepared with high purity (HP-Mg_2Si) and low purity (LP-Mg_2Si). For HP-Mg_2Si, Mg (5N-grade, Osaka Asahi Metal Mfg. Co., Ltd.) and Si (7N-up-grade, Furuuchi Chemical Co., Ltd.) were loaded into a pyrolytic graphite (PG)-coated graphite crucible with a stoichiometric ratio.[8,11,12)] For LP- Mg_2Si, Mg (3N-grade, Kojundo Chemical Laboratory Co., Ltd.) and Si (7N-up-grade, Furuuchi Chemical Co., Ltd.) were loaded into a BN-coated pBN crucible with a stoichiometric ratio.[9,11)] For the Sb- and Bi-doped crystals, Sb (6N-grade, Osaka Asahi Metal Mfg. Co., Ltd.) or Bi (5N-grade, Kojundo Chemical Laboratory Co., Ltd.) in addition to Mg (4N-grade, Rare Metallic Co., Ltd.) and Si (5N-grade, Kojundo Chemical Laboratory Co., Ltd.) was loaded in the molar ratio of <3at% into a BN-coated alumina crucible.[26)] These crucibles were then capped with carbon and placed in purified quartz ampoules. The ampoules were evacuated under a high vacuum ($<6\times10^{-6}$ Torr) and then sealed under Ar gas (560 Torr at 300 K) to prevent Mg evaporation during growth. In the VB growth, the growth ampoule was heated to 1363 K in a three-zone controlled resistance heating furnace. After holding at the temperature for 1-2 h, the ampoule was pulled down at a speed of 10 mm/h to grow a single-crystalline Mg_2Si bulk. After growth, the Mg_2Si bulk was cut perpendicular to the growth direction for analysis. The samples for Raman spectroscopy, X-ray fluorescence analysis (XRF), and electron probe microanalysis (EPMA) were lapped on one side and then mirror-polished with anhydrous fumed silica (Akasel A/S) and dehydrated ethanol.[27)]

2.2 Characterization of crystals

The amount of impurities in the samples was evaluated by XRF (ZSX Primus II, Rigaku) and EPMA. The carrier concentration was evaluated by Hall effect measurement with the van der Pauw method after cutting the substrate into 3 mm squares. The lattice constant was determined by Rietveld analysis of powdered X-ray diffraction (Ultima IV, Rigaku). High-purity Si powder was mixed in the samples as an internal standard and used to calibrate the lattice constant at 298 K. Raman spectroscopy (LabRAM HR Evolution, HORIBA) was performed on the polished surface, using a backscattering configuration because Mg_2Si is opaque to visible light. The measurement conditions were as follows: room temperature, a 633 nm He-Ne excitation light source, a 100x objective lens, and 10% dimming (1.7 mW), 10s exposure time, 3 integrations, and wavenumber range 100-400 cm^{-1}. The Raman spectra were measured at three points to check the variation of each measurement point. For all samples, the variation in peak positions was confirmed to be within ±0.15 cm^{-1}, below the wavenumber resolution of the instrument. Raman spectra were fitted in the wavenumber range of 200-300 cm^{-1} using the least squares method with the Lorentzian function. The amount of impurities in the samples used in the Raman spectroscopy measurement was accurately evaluated by EPMA.

2.3 Computational method

To investigate the relationship between the lattice strain and the Raman peak shift in Mg_2Si, we performed structural relaxation calculations by introducing impurities into a Mg_2Si supercell and phonon dispersion calculations by applying strain to the Mg_2Si unit cell. Both calculations were performed using density functional theory (DFT) calculations based on the Perdew-Burke-Ernzerhof (PBE) generalized gradient approximation (GGA)[28,29] using the Quantum ESPRESSO package[30], where the semi-localized normal-conserving pseudopotential (NCPP(SL)) was used. For the structural relaxation calculations with impurities, 2×2×2 and 3×3×3 supercells were constructed. These contain 96 atoms (64 Mg atoms and 32 Si atoms) and 324 atoms (216 Mg atoms and 108 Si atoms), respectively. One Si atom was substituted with Sb or Bi since both Sb and Bi have low formation energies for substitution at the Si site.[5] For the 2×2×2 supercell, the kinetic energy cutoff for the plane wave expansion of the electronic wavefunction was set to 50 Ry, and the Brillouin zone integration was performed with the 2×2×2 Monkhorst-Pack set. For the 3×3×3 supercell, the kinetic energy cutoff was set to 35 Ry, and the Brillouin zone integration was performed with the 1×1×1 Monkhorst-Pack set. For the calculation of the phonon dispersion, density functional perturbation theory (DFPT) was employed using a primitive cell to reduce computational cost. The lattice parameter was set within ±1% of the experimentally reported value for Mg_2Si (6.351 Å). The valence band wavefunctions were expanded in a plane wave prescribed set with a cutoff energy up to 50 Ry. The integration over the Brillouin zone was performed using the 7×7×7 Monkhorst-Pack set, giving 20 symmetrized k-points in the irreducible Brillouin zone. Winmostar version 11 (Cross Ability, Japan) was used as the GUI for calculations.

3. Results and discussion

Fig.1 (a) shows the relationship between dopant concentration in the fabricated crystals and prepared dopant amounts. It was found that the dopant concentration increased in proportion to the prepared dopant amount, and Sb concentration was higher than that of Bi at the same prepared dopant amounts. This indicates that Sb is more easily incorporated into Mg_2Si than Bi, which is in good agreement with previous experimental reports$^{3-5)}$. This result comes from the difference of the formation energy. Because the order of atomic radius is Si < Sb < Bi, it is presumed that the substitution with Bi causes a larger lattice strain than Sb, resulting in a larger formation energy. In fact, the previous reports demonstrated that the formation energy of Bi-doped Mg_2Si was higher than that of Sb-doped Mg_2Si by first-principles calculations$^{3-5)}$. Fig.1 (b) shows that the carrier concentration monotonically increased with the dopant concentration. The slope of the carrier concentration becomes especially slower when the Sb concentration exceeds about 0.5%. This would be attributed to the occupation of interstitial sites by Sb, reducing the activation rate. Therefore, it is suggested that the solubility limit at the Si-substitutional site may have already been reached at a dopant concentration of 0.5%. The solubility limit in single crystals was found to be lower than the previously reported values of ≥2 at.% for Sb-doped sintered bulk$^{4)}$, 2.3 at.% for Sb-doped thin films$^{31)}$, and 1.3 at.% and 2.3 at.% for Bi-doped sintered bulk materials.$^{3,32)}$ Fig.1 (c) shows the 2θ-ω scans of XRD around the 220 diffraction peak of Mg_2Si for undoped, Sb-doped (2%), and Bi-doped (2%) Mg_2Si samples. The 220 diffraction peak was shifted to the lower angle side by the addition of Sb and Bi, indicating an increase in the lattice constant. This is in good agreement with the experimental results in Ref. 33, where lattice constants are determined from XRD patterns. Fig. S1 shows the XRD pattern for the entire range. The experimental and calculated patterns showed good agreement for all samples. As a representative example, the fitting results for the Sb-doped (2%) sample are provided in Supplementary Table S1, where R_{wp} = 13.8% and R_{p} = 10.4%. The lattice constants calculated from the XRD patterns are presented in Fig. 1(d). Here, lattice strain is defined as the relative change in the lattice constant, calculated as $(a - a_0) / a_0 \times 100$ [%], where "a" is the measured lattice constant and "a_0" = 6.351Å is the reference value. With this definition, a positive value indicates expansion (an increase in the lattice constant), while a negative value indicates contraction (a decrease in the lattice constant). The results indicate that the lattice constant of the Mg_2Si single crystal increases with the dopant concentration, which is consistent with the previous reports on the Sb-doped thin film[31] and the Bi-doped sintered bulks.[32] In addition, the lattice constant of Bi-doped samples was larger than that of Sb-doped samples, which can be attributed to the larger atomic radius of Bi compared to Sb.

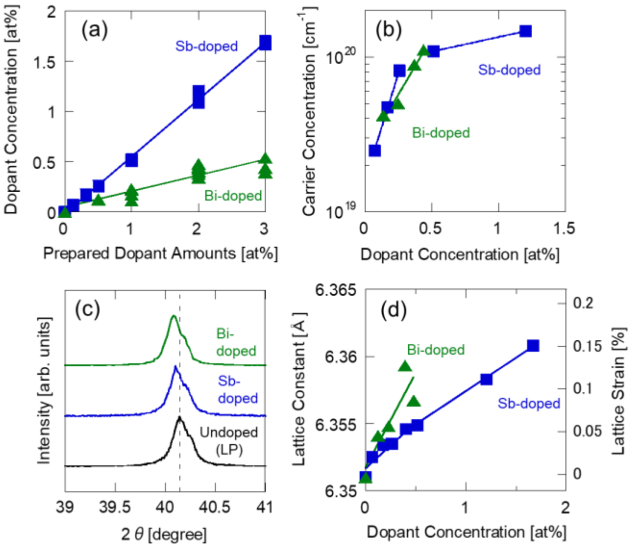

Fig.1. The results of structural characterization for undoped, Sb-doped and Bi-doped Mg_2Si. (a) Dopant concentration determined by XRF as a function of prepared dopant amounts. (b) Dopant concentration dependences of carrier concentration. (c) XRD patterns around the 220 diffraction peak for undoped, Sb-doped (2%) and Bi-doped (2%) Mg_2Si. (d) Dopant concentration dependences of lattice constant. The lines in (a), (b), and (d) represent linear approximations. The smaller peak shift observed in Sample #6 (Sb 1.08%) may suggest the introduction of dislocations through doping beyond the solid solubility limit, as shown in Figure 1(b) and (d). Furthermore, the observed relaxation of FWHM broadening could potentially be attributed to possible mechanisms including ordered arrangement of dislocations or their interactions with other crystal defects, though further investigation is required to confirm these hypotheses.

Fig.2 shows the Raman spectra of undoped, Sb-doped, and Bi-doped samples. These are the typical spectra among the three measured points. Each spectrum was normalized by the maximum intensity. Here, #1 is HP-Mg_2Si, and #2 is LP-Mg_2Si. In Fig. 2 (a)-(c), an F_{2g} peak is observed at around 258 cm^{-1} for all samples, and an F_{1u}(LO) peak is also observed at around 340 cm^{-1} for #2-8 samples. An F_{1u}(TO) peak also appeared near 280 cm^{-1} in #2. These are typical Raman spectra and are in good agreement with previous reports.[17-25] Here, the F_{2g} mode is a Raman-active vibration that is triply degenerate with the symmetric displacement of Mg and Si atoms.[20] The F_{1u} mode is split into a TO mode (~280 cm^{-1}) and a LO mode (~340 cm^{-1}). In this mode, the two Mg atoms adjacent to the Si atom are each displaced in the same direction[20,21]. Although the mode is usually infrared active, it can be observed as a Raman spectrum by the Frohlich interaction, which is attributed to crystalline symmetry breaking[21]. This indicates that the HP-Mg_2Si (#1) exhibits higher symmetry than the other samples. Figures 2 (d)-(f) show that the F_{2g} peak shifts to lower wavenumbers from that of the #1 sample (black dashed line) by doping Sb or Bi. These results are discussed in detail below by fitting the raw spectra with the Lorentzian function indicated by the red lines in Figs. 2(d)-(f).

Table 1 shows the dopant concentration revised by EPMA for Raman spectroscopy and the peak positions obtained by fitting the raw spectra. The peak position of 258.7 cm^{-1} for #1 and #2 samples is similar to previous reports (257[34], 258.3[19], 259[24] cm^{-1}).

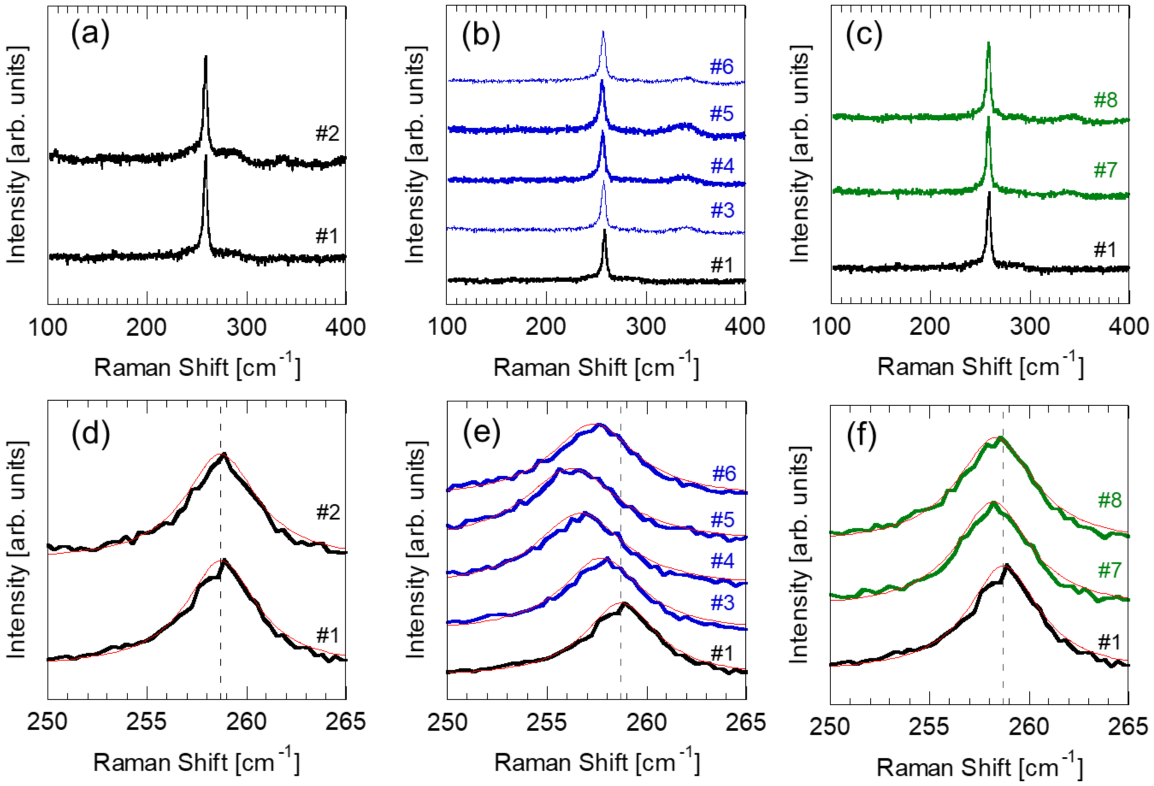

Fig.2. Raman spectra of (a) undoped, (b) Sb-doped, (c) Bi-doped samples. (d)-(f) Enlarged view of the area around 258 cm^{-1} for (a)-(c), respectively. The red lines in (d)-(f) indicate the fitting curve. The black dashed lines represent the peak position of #1 sample.

Table 1. Dopant concentration and peak position of each sample for Raman spectroscopy

Sample	Dopant		Peak Position
	Element	Concentration [at%]	[cm^{-1}]
#1	-	<0.01	258.7±0.06
#2	-	<0.01	258.7±0.02
#3	Sb	0.40	257.7±0.03
#4	Sb	0.67	256.7±0.14
#5	Sb	0.96	256.2±0.06
#6	Sb	1.08	257.4±0.03
#7	Bi	0.26	258.2±0.07
#8	Bi	0.29	258.3±0.09

To clarify the cause of the low wavenumber shift of the F_{2g} peak near 258 cm^{-1}, the peak position and full width at half maximum (FWHM) were plotted against dopant concentration as shown in Fig.3 (a) and (b), respectively. The black lines represent linear approximations using all data points. As the dopant concentration increased, the peak position shifted to the low wavenumber side, and the FWHM broadened.

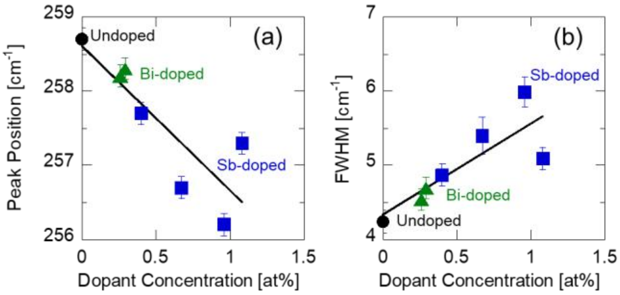

Fig. 3. (a) Peak positions and (b) FWHM against dopant concentration. The black line shows a linear fit through all the data points.

It is known that the peak shift of the Raman spectrum varies with temperature and strain.[15,16] Especially in silicon and diamond, tensile strain widens interatomic distances, weakens bonding forces, and reduces vibrational energy, resulting in a shift to lower wavenumbers.[15] If the strain is anisotropic or localized in the crystal, it is difficult to predict the wavenumber shift of the Raman spectrum. Therefore, we investigated the lattice strain of Sb- and Bi-doped Mg_2Si by lattice relaxation calculations using supercell structures of 2×2×2 and 3×3×3. Since it has been reported that Sb or Bi is substituted at the Si site in Mg_2Si[33], the calculations in this study were performed assuming substitution at the Si site. As shown in Table 2, when the Si site was substituted with Sb or Bi, the overall lattice length, labeled as "a", increased after structural optimization. (See Fig. S2 for definition of each character.) The overall lattice length of $Mg_{64}Si_{31}Sb$ and $Mg_{64}Si_{31}Bi$ was found to be enlarged by +0.22% and +0.30%, respectively, compared to $Mg_{64}Si_{32}$. Similarly, those of $Mg_{216}Si_{107}Sb$ and $Mg_{216}Si_{107}Bi$ were enlarged by +0.05% and +0.07%, respectively. The direction of this strain follows the same trend as the experimental results. Here, we also discuss the local lattice strain. The interatomic distance between the impurity and the nearest atom (Mg), labeled as d_{imp}, was +5.95% for $Mg_{64}Si_{31}Sb$ and +7.16% for $Mg_{64}Si_{31}Bi$, respectively, compared to $Mg_{64}Si_{32}$. Similarly, it was +6.08% for $Mg_{216}Si_{107}Sb$ and +7.26% for $Mg_{216}Si_{107}Bi$. These results are close to the experimental and calculated results presented in Ref. 33. The average of all bond lengths, labeled as $\bar{d}$, was +0.20% for $Mg_{64}Si_{31}Sb$ and +0.32% for $Mg_{64}Si_{31}Bi$, respectively. Similarly, they were +0.04% and +0.07% for $Mg_{216}Si_{107}Sb$ and $Mg_{216}Si_{107}Bi$, respectively. A histogram of all bond lengths is shown in Fig. S3. Extreme cases of significantly elongated bond length correspond to the impurity nearest neighbor bonds (d_{imp}), indicating that impurity nearest neighbor bonds are under high strain. Furthermore, it can be observed that other bond lengths are also distorted due to the strain caused by the impurities. Nevertheless, the average of each bond length ($\bar{d}$) is very close to the overall strain. This is the basis for the discussion below in terms of overall lattice strain. Notably, in a 3×3×3 supercell, the small difference in $\bar{d}$ arises from the reduced proportion of impurity atoms. The standard deviation of each bond length, labeled as σ_d, increased significantly with impurity substitution. In Lorentzian functions, while the standard deviation remains mathematically undefined, the FWHM exclusively governs the distribution broadening. This arises from FWHM's inherent role as the sole experimentally measurable and theoretically rigorous width parameter, effectively superseding standard deviation in practical spectral analysis. This DFT calculations supports the FWHM broadening in Figure 3(b).

To confirm the validity of the above calculation, the formation enthalpy was also calculated from the total energy using the following equation.[36)]

$$H_{form} = \frac{E_{tot} - N_{Mg}E_{solid}^{Mg} - N_{Si}E_{solid}^{Si} - N_{Sb}E_{solid}^{Sb}}{N_{Mg} + N_{Si} + N_{Sb}} \tag{1}$$

In the above equation, E_{tot} represents the total energy of the unit cell. N_{Mg}, N_{Si}, and N_{Sb} represent the number of Mg, Si, and Sb atoms in the unit cell model. E_{solid}^{Mg}, E_{solid}^{Si}, and E_{solid}^{Sb} represent the average single-atom energies of Mg, Si, and Sb atoms in the solid state, respectively. The Bi-doped model was also calculated in the same way. The calculated enthalpy values obtained in this study are in good agreement with those reported in other related studies.[36,39)] This suggests that the calculation methods and models are valid and the results are reliable.

Table 2. Lattice strain and enthalpy due to impurities; "a" is the overall lattice length, "d_{imp}" is the distance between the impurity and its nearest neighbor, "$\bar{d}$" is the mean of all bond lengths, "σ_d" is the standard deviation of bond lengths, and "H_{form}" is the enthalpy

of formation.

Models	a [Å]	d_{imp} [Å]	$\bar{d}$ [Å]	σ_d [Å]	H_{form} [kJ/mol]
$Mg_{64}Si_{32}$	12.698	2.749	2.749	2.2×10^{-6}	-22.69
$Mg_{64}Si_{31}Sb$	12.726 (+0.22%)	2.913 (+5.95%)	2.755 (+0.29%)	3.1×10^{-2}	-23.05
$Mg_{64}Si_{31}Bi$	12.736 (+0.30%)	2.946 (+7.16%)	2.758 (+0.32%)	4.0×10^{-2}	-22.45
$Mg_{216}Si_{108}$	19.029	2.747	2.747	2.2×10^{-6}	-21.80
$Mg_{216}Si_{107}Sb$	19.039 (+0.05%)	2.914 (+6.08%)	2.748 (+0.04%)	2.1×10^{-2}	-21.93
$Mg_{216}Si_{107}Bi$	19.042 (+0.07%)	2.946 (+7.26%)	2.748 (+0.07%)	2.4×10^{-2}	-21.76

Fig. 4 (a) shows the phonon dispersions when a uniform strain is applied to the unit lattice. Table 3 also shows the wavenumber of each mode at the Γ point. In Fig.4 (a), the F_{2g} mode at the Γ point shifts to the low and high wavenumber side when the lattice is expanded and contracted, respectively. The F_{1u} mode also shows a similar trend. Table 3 shows that the amount of F_{1u} mode shift is larger than that of the F_{2g} mode in both cases. This is consistent with the results for $Mg_2Si_{1-x}Sn_x$.24) This suggests that the F_{1u}(LO) mode is sensitive to strain and that it may be useful to discuss it in this context. However, when the symmetry is high, the F_{1u}(LO) peak does not appear, and even if it appears, its intensity is small. Therefore, it is not suitable for evaluating strain of single-crystalline Mg_2Si.

Fig.4 (b) shows the shift amount of the F_{2g} peak against lattice strain. The orange plus markers are calculated values using the previously reported data measured at low temperature19) and the lattice constant formula35) as follows:

$$a = 6.3272 + 8.5 \times 10^{-5}T + 3.8 \times 10^{-8}T^2 \tag{2}$$

where a is the lattice constant (unit: Å) and T is the absolute temperature (unit: K).

From Fig. 4 (b), the experimental shift of the F_{2g} peak exhibits a similar trend to that of the first-principles calculation, indicating that the experimental Raman shift is most likely due to lattice strain. Considering that the experimental value was slightly shifted larger, impurities might also be introduced into the interstitial sites or the presence of interfaces might cause large local strain.

From the above discussion, it is expected that it would be possible to evaluate lattice strain by observing the shift in the F_{2g} peak for single-crystalline Mg_2Si substrates.

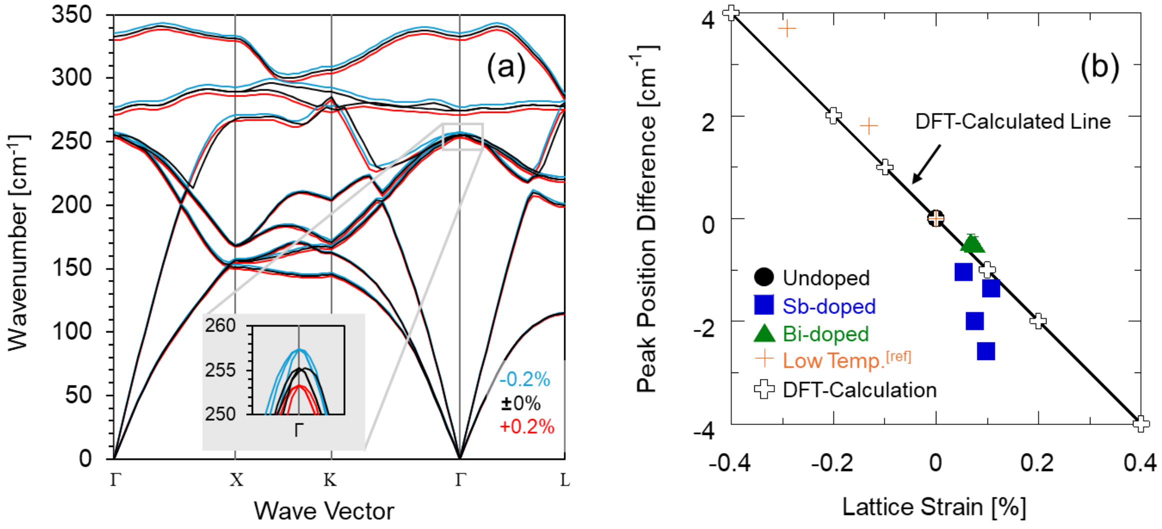

Fig. 4. (a) Phonon dispersions when the Mg_2Si unit cell is strained by ±0.2%. (b) Peak position difference versus lattice strain. The orange markers are calculated values from the previously reported data in Ref. 19 and eq. (2)

Table 3. The wavenumber of each mode at the Γ point

Strain [%]	F_{2g} [cm^{-1}]	F_{1u}(TO) [cm^{-1}]	F_{1u}(LO) [cm^{-1}]
-0.2	257.4	277.3	335.7
0	255.3	274.4	333.1
+0.2	253.3	271.1	330.2

4. Conclusions

Sb- and Bi-doped Mg_2Si single crystals were prepared by the vertical Bridgman techniques, and their Raman spectra were analyzed in detail. The dopant concentration increased in proportion to the prepared dopant amount, and Sb concentration was higher than that of Bi at the same amounts. Rietveld analysis of powder XRD revealed that the lattice constant increased monotonically with increasing Sb and Bi doping amounts. While F_{2g} peak of Raman spectra is observed at around 258 cm^{-1} for all samples, an F_{1u}(LO) peak is also observed at around 340 cm^{-1} for LP-Mg_2Si, and impurity-doped samples. This indicates that

LP-Mg_2Si and impurity-doped samples exhibits low crystalline symmetry. In addition, the F_{2g} peak of Raman spectra (near 258 cm^{-1}) of Sb- and Bi-doped Mg_2Si exhibited a shift to lower wavenumbers with increasing doping. This peak shift was attributed to the lattice strain, which was revealed by the First-principles calculations. These findings provide the usefulness of Raman spectroscopy for Mg_2Si substrates.

Supplementary Material

The supplementary material includes the full-range XRD patterns, the definitions of parameters in the supercell of Mg_2Si, and histograms of bond lengths "*d*.".

Acknowledgments

This work was supported by Grants-in-Aid for Scientific Research (B) under Grant No. 23H01440 from JSPS KAKENHI, Japan, and the Adaptable and Seamless Technology Transfer Program (A-STEP) under Grant Nos. JPMJTR21RB and JPMJTR22R3 from the Japan Science and Technology Agency (JST). The authors thank Mitsuaki Nishio of the National Institute for Materials Science (NIMS) for EPMA, and Megumi Sato of NIMS for experimental support. This study was partially supported by a Grant-in-Aid for Scientific Research (KAKENHI) (grant number JP22H00268) from the Japan Society for the Promotion of Science (JSPS). The authors also thank S. Hasunuma, H. Otake, and T. Otsubo, former students of our laboratory, for their contributions to XRF, Hall effect measurements, and powder XRD measurements of Sb-doped and Bi-doped Mg_2Si single crystals.

References

1) S. Tada, Y. Isoda, H. Udono, H. Fujiu, S. Kumagai, and Y. Shinohara, Phys. Status Solidi C **10**, 1074 (2013).

2) K. Kambe and H. Udono, J. Electron. Mater. **43**, 2212 (2014).

3) J. Tani and H. Kido, Physica B **364**, 218 (2005).

4) J. Tani and H. Kido, Intermetallics **15**, 1202 (2007).

5) J. Tani and H. Kido, Intermetallics **16**, 418 (2008).

6) R. G. Morris, R. D. Redin, and G. C. Danielson, Phys. Rev. **109**, 1909 (1958).

7) M. W. Heller and G. C. Danielson, J. Phys. Chem. Solids **23**, 601 (1962).

8) D. Tamura, R.Nagai, K. Sugimoto, H. Udono, I. Kikuma, H. Tajima, and I. J. Ohsugi, Thin Solid Films **515**, 8272 (2007).

9) R. Masubuchi, B. Alinejad, Y. Hara, H. Udono, Crystal Growth **571**, 126258 (2021).

10) S. Sakane and H. Udono, AIP Advances **13**, 105307 (2023).

11) H. Udono, H. Tajima, M. Uchikoshi, and M. Itakura, Jpn. J. Appl. Phys. **54**, 07JB06 (2015).

12) T. Tokairin, J. Ikeda, and H. Udono, Crystal Growth **468**, 761 (2017).

13) H. Udono, Y. Yamanaka, M. Uchikoshi, and M. Isshiki, Phys. Chem. Solids **74**, 311 (2013).

14) T. Akiyama, N. Hori, S. Tanigawa, D. Tsuya, and H. Udono, JJAP Conf. Proc. **5**, 011102 (2017).

15) D. Tuschel, Spectroscopy **34**(9) (2019).

16) T. Uchida, T. Masuyama, R. Sugie, and S. Watanabe, Microelectronics Reliability **121**, 114132 (2021).

17) W. B. Whitten, P. L. Chung, and G. C. Danielson, Phys. Chem. Solids **26**, 49 (1965).

18) L. Laughman and L. W. Davis, Solid State Communications **9**, 497 (1971).

19) C. J. Buchenauer and M. Cardona, Phys. Rev. B, **3**(8), 2504 (1971).

20) E. Anastassakis and C. H. Perry, Phys. Rev. B, **4**(4), 1251 (1971).

21) S. Onari and M. Cardona, Phys. Rev. B, **14**(8) (1976).

22) S. Onari, M. Cardona, E. Schonherr, and W. Stetter, Phys. Stat. Sol. (b) **79**, 269 (1977).

23) J. L. Wang, S. J. Zhang, Y. Liu, C. Q. Jin, N. N. Li, L. J. Zhang, Q. J. Liu, R. Shen, Z. He, and X. R. Liu, J. Phys. D: Appl. Phys. **50**, 235304 (2017).

24) M. Yasseri, D. Schüpfer, L. Chen, H. Kamila, E. Müller, J. d. Boor, and P. J. Klar, Phys. Status Solidi RRL **14**, 1900574 (2020).

25) Y. Liao, M. Fan, Q. Xie, Q. Xiao, J. Xie, H. Yu, S. Wang, and X. Ma, Applied Surface Science **458**, 360 (2018).

26) M. Akasaka, T. Iida, T. Nemoto, J. Soga, J. Sato, K. Makino, M. Fukano, and Y. Takanashi,

Crystal Growth **304**, 196 (2007).

27) T. Suemasu, K. O. Hara, H. Udono, and M. Imai, J. Appl. Phys. **131**, 191101 (2022).

28) J. P. Perdew, K. Burke, M. Emzerhof, Physical Revew Letters, **77**(18), 3865 (1996).

29) P. Pandit and S. Sanyal, Indian J. Pure & Appl. Phys. **49**, 692 (2011).

30) P. Giannozzi et al., "Quantum ESPRESSO: a modular and open-source software project for quantum simulations of materials", arXiv:0906.2569 (2009).

31) C. Prahoveanu, A. Locoste, C. d. Vaulx, K. Azzouz, M. Salaun, Y. Liu, D. Tainoff, O. Bourgeois, and L. Laversenne, Journal of Alloys and Compounds **688**, 195 (2016).

32) A. Kolezynski, P. Nieroda, P. Jelen, M. Sitarz, and K. T. Wojciechowski, Vibrational Spectroscopy **76**, 31 (2015).

33) M. Kitaura, S. Watanabe, T. Ina, M. Imai, H. Udono, M. Ishizaki, H. Yamane, T. Tanimoto, and A. Ohnishi, J. Appl. Pys. 130, 245105 (2021).

34) T. Ikehata, T. Ando, T. Yamamoto, Y. Takagi, N.Sato, and H. Udono, Phys. Status Solidi C 10, No. 12, 1708 (2013).

35)H. Kasai, L. Song, H. L. Andersen, H. Yin, and B. B. Iversen, Acta Cryst. **B73**, 1158 (2017).

36) Y. Li, T. Ma, Y. Ren, T. Liu, and X. Xou, Mater. Res. Express **7**, 036533 (2020).

37) H. Balout, P. Boulet, and M. C. Record, Intermetallics **50**,8 (2014).

38) M. Baleva, G. Zlateva, A. Atanassov, M. Abrashev, and E. Goranova, Phys. Rev. B **72**, 115330 (2005).

39) H. Zhang, S. Shang, J. E. Saal, A. Saengdeejing, Y. Wang, L. Chen, and Z. Liu, Intermetallics **17**, 878 (2009).